

17 **Abstract (137)**

18 Underwater disturbances are the largest error source in GNSS-A seafloor geodetic observation.
19 In particular, the gradient of sound speed structure directly affects the horizontal accuracy and
20 needs to be examined. Previous studies have not investigated its temporal change component. In
21 this paper, we verified the assumption that the underwater gradient structure does not change
22 significantly during GNSS-A observation for several hours through applying a modified version
23 of an analysis software called GARPOS to actual data of SGO-A (provided by Japan Coast
24 Guard). Obtained results suggested that this assumption holds at many observation data, and the
25 positioning accuracy becomes better. Some non-improved observation epochs were speculated to
26 be accompanied by structure changes for which this assumption was not valid. It is suggested
27 that the sound speed structure change during observation will be an important research topic in
28 GNSS-A.

29 **Plain Language Summary (140)**

30 GNSS-A is a seafloor geodetic observation method that determines the seafloor position by
31 combining Global Navigation Satellite System (GNSS) and acoustic ranging with centimeter-
32 scale accuracy. The biggest error in GNSS-A is not the high-rate (> 1 Hz) GNSS noise, but the
33 kilometer-scale underwater disturbances. Previous studies have showed that the gradient of the
34 sound speed structure strongly affects the positioning accuracy, but its time stability has not been
35 verified. This paper has verified the assumption that the underwater structure does not change
36 significantly during several hours in GNSS-A observation and only the intensity of the gradient
37 may change. Incorporating this assumption into the analysis method improved the variation of
38 the GNSS-A time-series. Thus, the kilometer-scale underwater structure was found to be
39 generally time-stable for components that affect GNSS-A. This leads new research theme of
40 GNSS-A seafloor geodesy and GNSS-A oceanography.

42 **1 Introduction**

43 In the last 15 years, many kinds of geophysical phenomena have been detected by a seafloor
44 geodetic monitoring technique called as the Global Navigation Satellite System (GNSS) -
45 Acoustic ranging combination technique (GNSS-A) proposed in 1980s (Spiess, 1985; Asada and
46 Yabuki, 2001; Fujita et al., 2006) (fig. 1a). GNSS-A determines a seafloor position by combining
47 high-rate (> 1 Hz) GNSS and underwater acoustic ranging on a sea surface platform such as a
48 vessel.

49 Although the uncertainty of GNSS-A positioning data differs at each observation site, the
50 standard deviation in the horizontal components (σ) is empirically about 2.0 cm and 1.5 cm in
51 the best case in data of the GNSS-A Seafloor Geodetic Observation Array (SGO-A), provided by
52 Japan Coast Guard (JCG) (Yokota et al., 2018). GNSS-A with this accuracy can detect temporal
53 changes of crustal deformation by a transient postseismic effect, interplate coupling condition
54 changes, and slow slip events (e.g., Sato et al., 2011; Yokota et al., 2016; Yokota and Ishikawa,
55 2020; Watanabe et al., 2021a).

56 Because GNSS-A is a technique which combines the radio wave positioning and acoustic wave
57 positioning, the temporal and spatial inhomogeneity of the medium above and under the water
58 affects the accuracy. In this paper, we focus on acoustic medium i.e., sea water. Oceanographic
59 disturbance causing variations in under water sound speed structure (SSS) is one of the major
60 error sources of GNSS-A. To observe the temporal change of crustal deformation, which has
61 been actively studied in recent years (Yokota et al., 2021), the positioning accuracy of 1 cm or
62 less is required. Therefore, high-accuracy estimation of SSS is indispensable for seismological
63 purpose of GNSS-A and various studies have been conducted (Yokota and Ishikawa, 2019;
64 Yokota et al., 2020; Kinugasa et al., 2020).

65 In the GNSS-A observation (fig. 1a) routinely operated by JCG, thousands of acoustic round-trip
66 travel time are measured between multiple seafloor stations (acoustic transponder) and a surface
67 station in a few hours to half a day. A surface station moves around the area where the horizontal
68 distance is about twice the water depth and performs acoustic ranging. Here, we use the open

69 source GNSS-A positioning software GARPOS, which enables high-precision and high-speed
 70 GNSS-A analysis (Watanabe et al., 2020; 2021b). GARPOS estimates the spatiotemporal
 71 variation of SSS in the observation area using the sufficiently many acoustic data collected from
 72 surface and seafloor stations' positions (fig. 1b).

73 In this paper, we examined the pattern of SSS estimated by GARPOS, using the actual data
 74 obtained at the Nankai Trough (ASZ2) and the Japan Trench (FUKU) (fig. 1c) (Japan Coast
 75 Guard, 2021), which have different ocean fields. In the Nankai Trough region (especially on its
 76 western side), the stable Kuroshio Current generates a stable SSS. On the other hand, in the
 77 Japan Trench region, SSS is more complex due to the mixing of warm water from Kuroshio and
 78 cold water from Oyashio.

79

80 **2 SSS estimation in GARPOS**

81 GARPOS estimates the model parameter (seafloor stations' positions and SSS as perturbations of
 82 travel time) using the residuals between observed acoustic travel time and calculated one. The
 83 round-trip travel time is calculated as a function of the seafloor stations' positions, \mathbf{X} , surface
 84 station's position, $\mathbf{P}(t)$, and 4-dimensional (4D) SSS, $V(e, n, u, t)$, where e , n , u , and t are
 85 eastward, northward, upward, and time components, respectively. However, since it is
 86 impossible to accurately grasp 4D-SSS, GARPOS (Watanabe et al., 2021b) estimates SSS's
 87 effect on travel time decomposing $V(e, n, u, t)$ into an effect from a horizontally stratified steady
 88 profile (reference SSS), $V_0(u)$, and a perturbation. $V_0(u)$ is obtained from sea water observation,
 89 such as Conductivity, Temperature, Depth sensors (CTD). This decomposition is expressed as
 90 following using travel time:

$$91 \quad T(V(e, n, u, t)) = \exp(-\gamma) \cdot \tau(V_0(u)), \quad (1)$$

92 where τ denotes the reference travel time obtained under $V_0(u)$, and γ expresses the effect of
 93 spatiotemporal variation of SSS from the reference. Since GNSS-A has measurement points on
 94 the sea surface and seafloor only, the correction term γ is picked up from a perturbation field
 95 expressed as a function of those positions, $\Gamma(t, \mathbf{P}, \mathbf{X})$. GARPOS version 1.0.0 implements Γ
 96 estimation using the following linear relations as a simple function:

$$97 \quad \Gamma(t, \mathbf{P}, \mathbf{X}) = \alpha_0(t) + \alpha_1(t) \cdot \mathbf{P} + \alpha_2(t) \cdot \mathbf{X}. \quad (2)$$

98 α_0 typically indicates the time-dependent coefficient for the average sound speed change. The
 99 coefficients for the second and third terms expresses the spatiotemporal variation of SSS
 100 depending on the surface and seafloor stations' positions.

101 $|\gamma| \ll 1$, where V_0 appropriately represents the actual SSS, is satisfied in most cases. In such
 102 cases, the deviation of actual ray path from the reference is small, so that the average sound
 103 speed along the actual path can be expressed as $\bar{V}_0 + \delta V_i \sim \bar{V}_0 + \gamma_i \bar{V}_0$, where \bar{V}_0 denotes the
 104 average of $V_0(u)$.

105 Fig. 2 shows the 2D schematic picture of the decomposition of SSS effect and its projection to
 106 the perturbation field, $\Gamma(t, \mathbf{P}, \mathbf{X})$. In the scheme of GARPOS, a contribution from the actual
 107 structure is lineally decomposed into ones from a steady reference profile and a residual
 108 structure. Residual structure causes a spatial variation in travel time of acoustic paths. The
 109 coefficients α_1 and α_2 in Γ are estimated from by this spatial variation in travel time.

110 Multiplying the \bar{V}_0 [m/s] by α_1 [km⁻¹] and α_2 [km⁻¹] gives characteristic gradient sound speed
 111 parameters, $\mathbf{g}_1(t)$ [m/s/km] and $\mathbf{g}_2(t)$ [m/s/km] to express the residual structure.

112 The representation of residual structure using \mathbf{g}_1 and \mathbf{g}_2 means that the bulk structure is
 113 projected onto functions in the boundary planes on the sea surface and seafloor. Rigidly, \mathbf{P} and \mathbf{X}
 114 have vertical fluctuations, but they are enough small compared to the water depth of the entire
 115 space, so they can be regarded as approximately flat surfaces. This “holographic projection”
 116 reflects the SSS as “shadow” on surface and seafloor planes.

117 Considering the 2D case, if a single uniform gradient layer exists at a certain depth as in fig. 2a
 118 (i.e., $\text{sign}(g_1) = \text{sign}(g_2)$), the characteristic depth (central depth) of the gradient layer, D_c , is
 119 expressed by the ratio ($\frac{g_1}{g_2}$) as the following equation (modified from eq. (32) in Watanabe et al.
 120 (2020)):

$$121 \quad \frac{D_c}{D} = \left(1 + \frac{g_1}{g_2}\right)^{-1}, \quad (3)$$

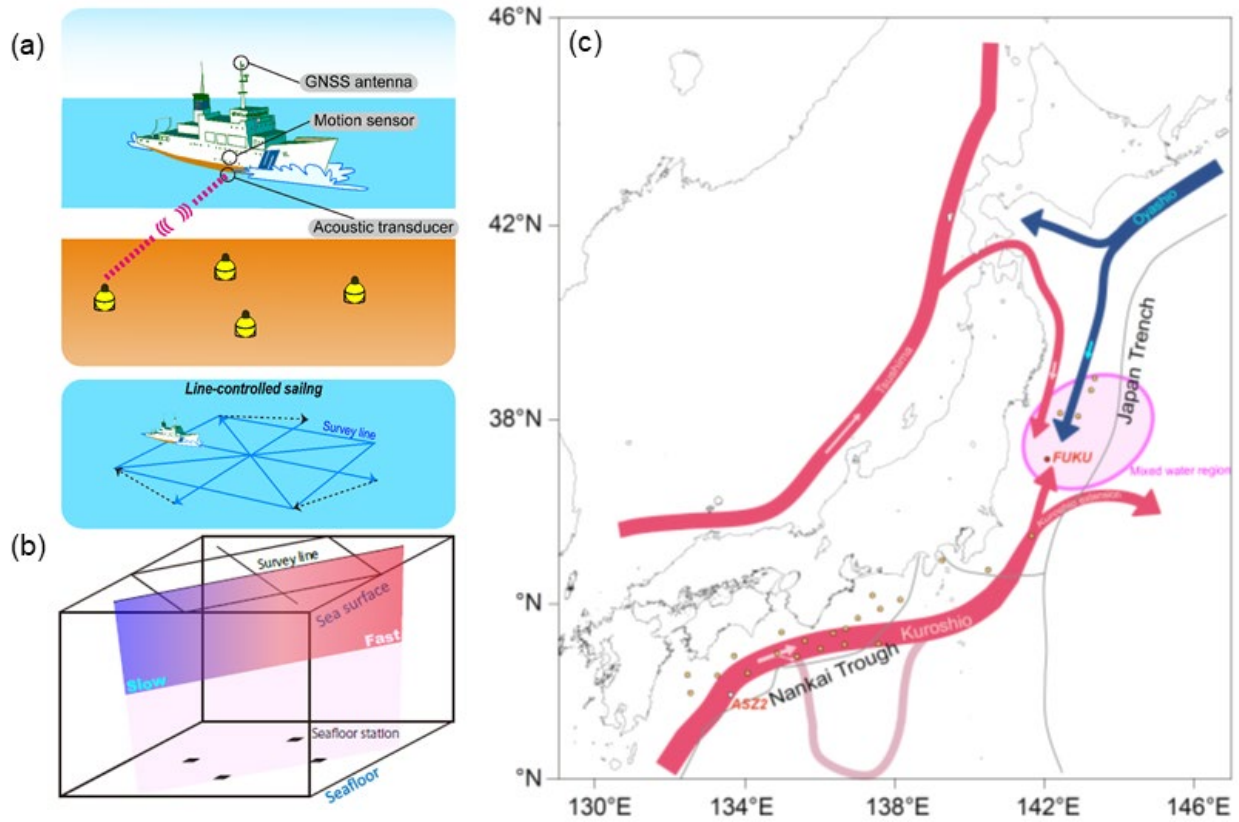
122 where D is a water depth. Because the full information of bulk SSS is partially lost by the
 123 projection to boundary, this projection is irreducible, i.e., it is not unique to inversely estimate
 124 SSS from g_1 and g_2 . It is not possible to distinguish between a thick weak gradient and a thin
 125 strong gradient at almost the same depth, both of which provide the same g_1 and g_2 (Yokota,
 126 2019). In complicated cases (fig. 2b) that cannot be assumed with a single gradient, the
 127 relationship between g_1 and g_2 becomes more complicated.

128 In actual case, \mathbf{g}_1 and \mathbf{g}_2 are contracted into 2D vectors with eastward and northward
 129 components, i.e., $\mathbf{g}_1 = (g_{1E}, g_{1N})$ and $\mathbf{g}_2 = (g_{2E}, g_{2N})$. To verify the 3D structure, we classify
 130 the relationship of g_{1d} and g_{2d} as $\mathbf{G}_d = (g_{2d}, g_{1d})$ ($d = E, N$) on the g_{2d} - g_{1d} plane as shown in
 131 the right side of fig. 2. Here, we can define the angle $\theta_{Gd} (= \arctan(\frac{g_{1d}}{g_{2d}}))$ as the characteristic
 132 state of SSS.

133 First, we consider the first and third quadrants ($\text{sign}(g_{1d}) = \text{sign}(g_{2d})$). These cases can be
 134 virtually interpreted as a single layer as fig. 2a and the characteristic depth D_c of gradient layer is
 135 expressed as eq. (3). We define these quadrants as Type-I. It is possible to interpret that the
 136 structure is a single gradient layer, though it can also be a complex situation with multiple
 137 gradient layers even for the same g_{1d} and g_{2d} (Yokota, 2019). The second and fourth quadrants
 138 ($\text{sign}(g_{1d}) \neq \text{sign}(g_{2d})$) cannot be interpreted as a single layer (Type-II). In this case, SSS
 139 contains multiple characteristic scales for temporal and spatial variation. For example, it is likely
 140 to be dominated by a temporary structure such as a water intrusion (fig. 2b), which typically
 141 cannot be approximated to a linear SSS in km-scale (as fig. 2b). Therefore, the simple Γ

142 expression defined as eq. (2) tends to be insufficient to reflect the Type-II structures, which is a
143 topic for future research.

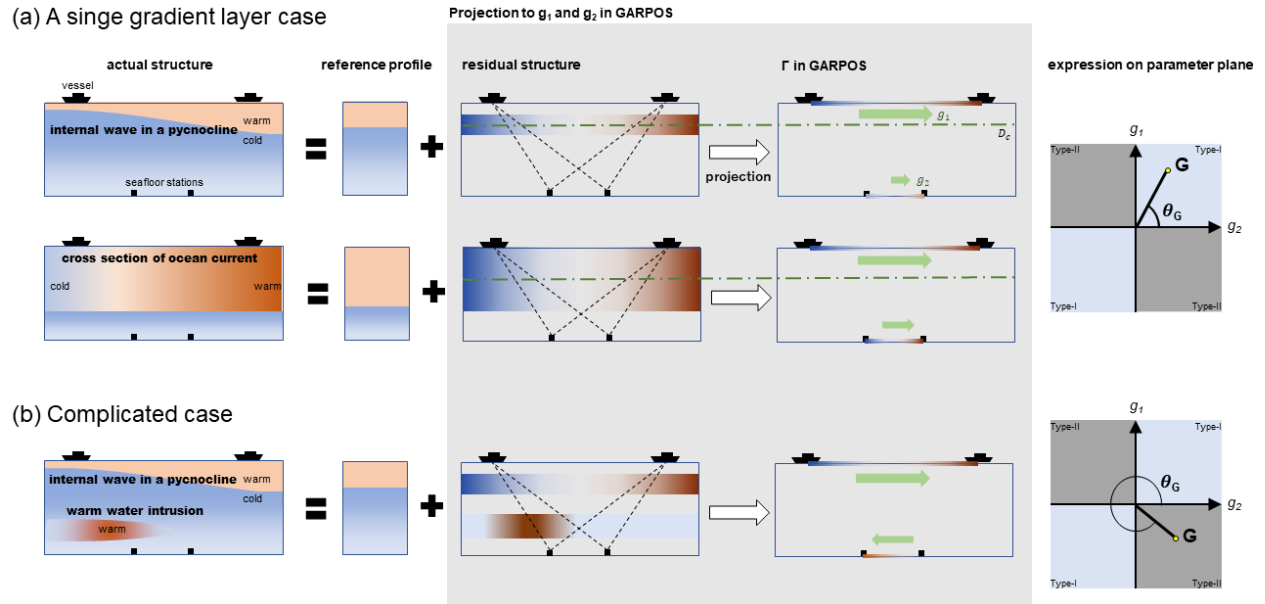
144



145 **Figure 1.** (a) A schematic of GNSS-A system (modified after Yokota et al. (2019)). (b) An
 146 example of gradient effect for the GNSS-A observation. Colored region indicates a projection of
 147 SSS on a plane. Colors indicated the sound speed. (c) The location of SGO-A sites. Currents
 148 (bold lines) and a mixed water region (purple region) are based on Yasuda et al. (1996).

149

150



151 **Figure 2.** Schematic diagrams of a holographic projection in GARPOS for (a) single layer cases
 152 and (b) a complicated case. (Right) Plots of $\mathbf{G} = (g_2, g_1)$ on the 2D g_2 - g_1 plane.
 153

154 **3 Constraint on \mathbf{G} trajectory**

155 Figs. 3a and 3b show the ASZ2 positioning time-series (northward component) estimated in
 156 GARPOS and the range of \mathbf{G}_N trajectories. Outliers in time-series (blue circles) are often located
 157 at boundaries across quadrants in the \mathbf{G}_N plane (blue-lined ellipses in fig. 3b). Figs. 3c–e show
 158 the \mathbf{G}_N trajectory examples of non-outlier (Jan. 2012, hereafter 2012-Jan) and outlier (2017-Jul
 159 and 2014-Sep) cases. In fig. 3c, \mathbf{G}_N fluctuates linearly within Type-I. On the other hand, in figs.
 160 3d and 3e, \mathbf{G}_N fluctuates linearly and non-linearly, respectively, and both cross the boundary of
 161 third quadrant.

162 The \mathbf{G}_d trajectories represent the temporal variation of SSS and are interpreted as shown in fig. 4.
 163 Fig. 4a shows the simplest case, occurring the internal gravity wave in a pycnocline that is the
 164 boundary between hot and cold water, the gradient layer is generated only at a certain depth. In
 165 this case, \mathbf{G}_d trajectory caused by internal wave travelling is a linear trend with constant θ_{Gd} as
 166 shown in the bottom of fig. 4a. In addition, existing a stable strong gradient field of $\theta_{Gd} = \theta_{Gd1}$
 167 (e.g., due to a current) as the background, the situation becomes as shown in fig. 4b. In this case,
 168 the \mathbf{G}_d trajectory is a linear trend with constant θ_{Gd2} , and not passing the origin of the \mathbf{G}_d plane.
 169 In this simple but realistic case, the trajectory is expected to be a linear line. For more
 170 complicated case, the trajectory is no longer expected to be a linear line. For example, when the
 171 water mass intrudes into another depth, a \mathbf{G}_d trajectory is complicated depending on the speed of
 172 the inflow (fig. 4c) and goes through Type-II that may not express the actual SSS appropriately.
 173 2012-Jan is close to fig. 4a or 4b and 2017-Jul and 2014-Sep are close to fig. 4c, respectively.

174 Here, we consider how the estimations of positions and SSS can be improved in these cases. The
 175 fluctuation of \mathbf{G}_d trajectory is considered to be affected by both actual SSS variation and error.
 176 In GARPOS, the bulk SSS is represented by two boundary functions \mathbf{g}_1 and \mathbf{g}_2 . Therefore, \mathbf{g}_1
 177 and \mathbf{g}_2 should be correlated to some extent. On the other hand, because \mathbf{g}_2 is strongly correlated
 178 with the seafloor station's position \mathbf{X} , the estimation of \mathbf{g}_2 is less robust than \mathbf{g}_1 due to the
 179 influence of unmodeled error sources. Therefore, the result is expected to be more reliable by
 180 adding the constraint between \mathbf{g}_1 and \mathbf{g}_2 , rather than treating them as independent parameters.

181 Based on the relationship between the outliers and \mathbf{G}_d shown in fig. 3, this study introduces the
 182 assumption corresponding to fig. 4a whose gradient depth does not change over time.

183 Because the actual SSS variation cannot be observed directly, we evaluated the validity of this
 184 assumption from the variation of the seafloor position time-series result in next section. A correct
 185 constraint condition should reduce the time-series variation.

186 Here, we consider constraining \mathbf{G}_d on a line passing through the origin with a constant slope of
 187 κ_d as fig. 4a. This corresponds to replacing eq. (2) as follows:

$$188 \quad \Gamma_2(t, \mathbf{P}, \mathbf{X}) = \alpha_0(t) + \boldsymbol{\alpha}_1(t) \cdot \mathbf{P} + (\kappa_E^{-1} \alpha_{1E}(t), \kappa_N^{-1} \alpha_{1N}(t), 0) \cdot \mathbf{X}. \quad (4)$$

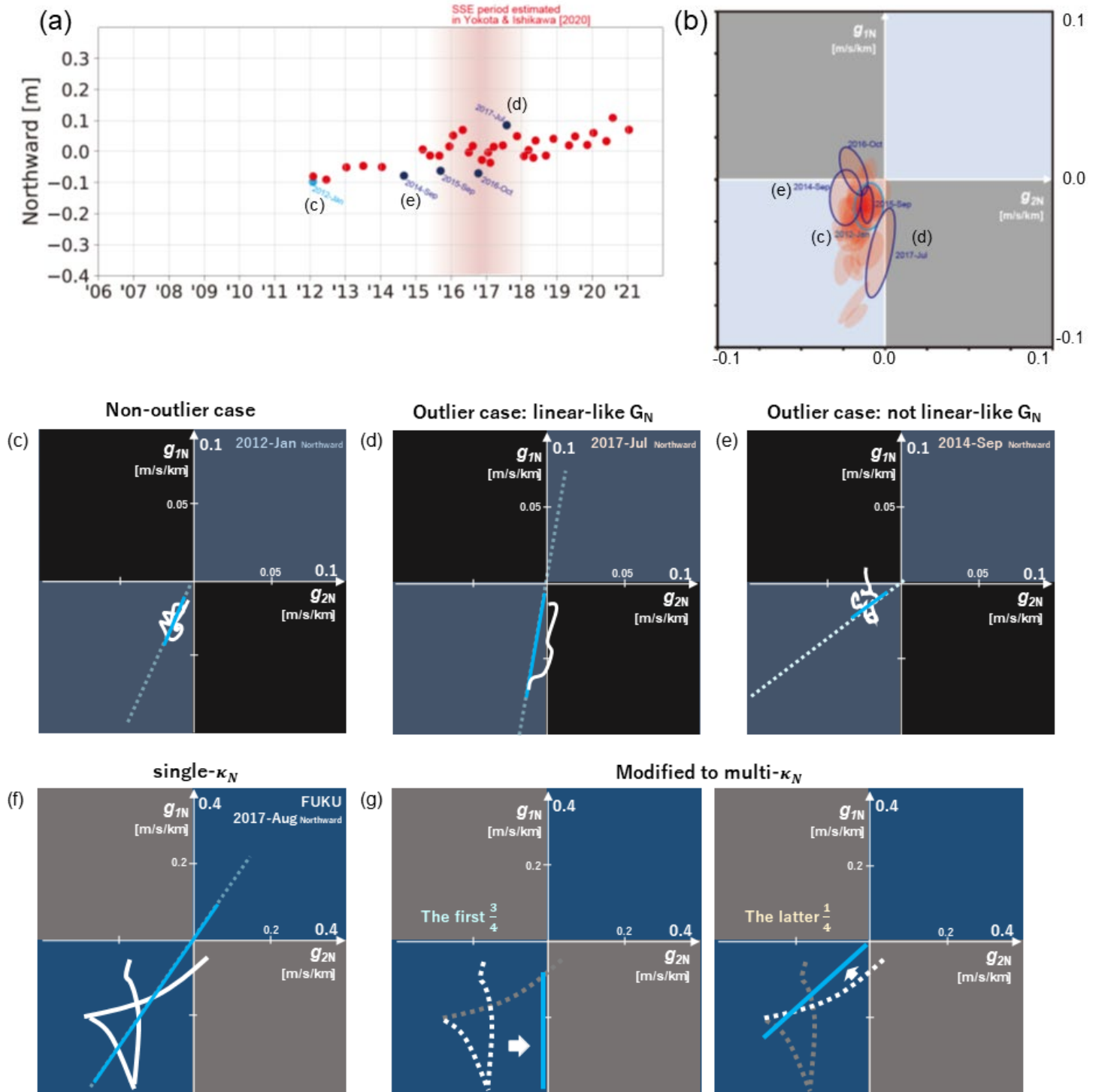
189 Because the GARPOS version 1.0.0 dose not support the formulation of eq. (4), we performed
 190 the following two-step algorithm: In the 1st-cycle, the same analysis as GARPOS was performed
 191 using Γ to determine κ_d using the \mathbf{G}_d trajectory (step-0). In the 2nd-cycle, the analysis using Γ_2
 192 was performed constraining κ_d estimated from the 1st-cycle result.

193 To determine κ_d after the 1st-cycle based on the above assumption, the following flow (fig. 5a)
 194 was tried:

195 When \mathbf{G}_d is within the Type-I range and does not straddle each quadrant, κ_d was determined
 196 from the median of θ_{Gd} (step-1; case-A). In other cases, to determine whether or not \mathbf{G}_d changes
 197 linearly, the fitting ellipse was estimated with respect to all \mathbf{G}_d parameters (step-2). If the semi-
 198 major axis length (a_L) of the estimated ellipse is more than an arbitrary ratio (p) with the semi-
 199 minor axis length (a_s), the semi-major axis direction was determined as κ_d (case-B). In this
 200 study, p was set to 4. For an epoch whose \mathbf{G}_d trajectory cannot be linearly approximated, κ_d was
 201 estimated from the median of θ_{Gd} (case-C). This operation was performed individually on the
 202 eastward and northward components.

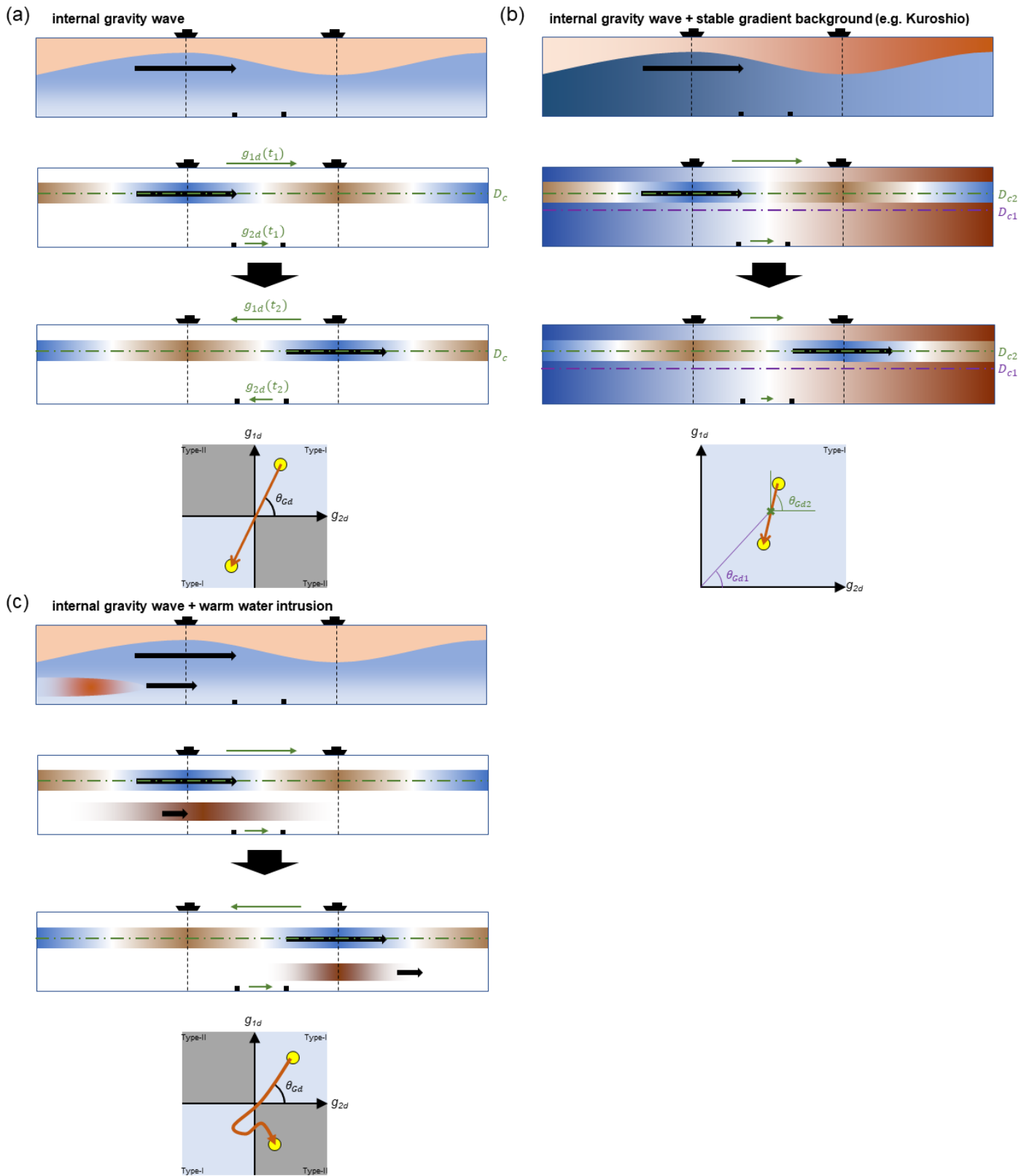
203

204 For example, 2012-Jan (fig. 3c) was classified in case-A, and κ_N was constrained on a dotted line
205 and \mathbf{G}_N was determined on a blue line. 2017-Jul (fig. 3d) was classified in case-B, \mathbf{G}_N , which was
206 displaced horizontally due to an unexpected error in the 1st-cycle, was corrected. 2014-Sep (fig.
207 3e) was classified in case-C, \mathbf{G}_N in the Type-II range was corrected. Here, each resultant acoustic
208 signal residual was almost unchanged and indistinguishable.
209



210 **Figure 3.** (a) The northward component of ASZ2 positioning time-series estimated in GARPOS.
 211 Pink region indicates a slow slip event period estimated in Yokota and Ishikawa (2020). Blue
 212 circles indicate outliers that deviate from the variation in surrounding epochs. Light-blue circle is

213 a non-outlier example. (b) Ellipses indicate the range of \mathbf{G}_N trajectories of all epochs. Blue-lined
214 ellipses indicate outlier cases in (a). Light-blue-lined ellipse indicates a non-outlier example. (c–
215 e) \mathbf{G}_N estimated in GARPOS (1st-cycle; white line) and the proposed 2nd-cycle (light-blue line)
216 on the $g_{2N}-g_{1N}$ plane. Dotted line indicates the κ_N direction. (f) \mathbf{G}_N of 2017-Aug at FUKU. (g)
217 \mathbf{G}_N estimated when the first $\frac{3}{4}$ data (left) and the latter $\frac{1}{4}$ data (right) were fixed to $\arctan(\kappa_N) = \frac{\pi}{2}$
218 and $\frac{\pi}{4}$, respectively.
219



220 **Figure 4.** Three types of temporal changes in gradient fields from t_1 to t_2 (a) due to an internal

221 gravity wave, (b) in addition, due to a stable gradient background, and (c) in addition, a water
222 intrusion. Each \mathbf{G}_d trajectory is drawn on the bottom.

223

224 **4 Application of assumption**

225 In this section, we verify the effect of constraint assumption, comparing the position time-series
226 and estimated \mathbf{G}_d . Figs. 5b and 5c compares the ASZ2 time-series and ranges of \mathbf{G}_d determined
227 in the 1st- and 2nd-cycles.

228 The case-A (dark-blue circle in fig. 5b) such as the case in fig. 3c is the major pattern in the both
229 components at ASZ2. In these cases, the variation of positioning solutions was improved by
230 constraining the fluctuation of \mathbf{G}_d . Outliers in the 1st-cycle time-series tend to have \mathbf{G}_d trajectory
231 straddling the Type-I and Type-II regions, i.e., in case-B or C, and the positioning solutions were
232 improved by confining \mathbf{G}_d . This result indicates that the straddling these regions is caused by the
233 error rather than the actual SSS variation and the constraint assumption leads a correct solution.
234 Because ASZ2 is often located in the Kuroshio (fig. 1c), the condition that the straight \mathbf{G}_d does
235 not pass through the origin strictly (fig. 4b) is expected rather than the given constraint.
236 Therefore, there may be constraints to obtain a better time-series than the constraint given in this
237 study (assuming fig. 4a).

238 For comparison, data of FUKU in the Japan Trench region (fig. 5b) was analysed with the same
239 settings. In this site, about 80% were determined in cases-B and C, and suggesting more
240 complicated sea conditions along the Japan Trench (fig. 1c) than ASZ2. κ_d were determined in
241 more various directions than ASZ2 (fig. 5c), suggesting that there was no steady background
242 SSS with strong gradient structure. FUKU results also showed the improvement in the variation
243 of time-series, except for some outliers.

244 The cases where \mathbf{G}_d was constrained on Type-II in the 2nd-cycle (pink-lined circles) should be
245 difficult to track SSS changes properly. However, even in those cases, there was no serious
246 deterioration of the positioning solution. There might have been no significant θ_{G_d} change during
247 the observation time. The analytical handling of such cases is a further research topic.

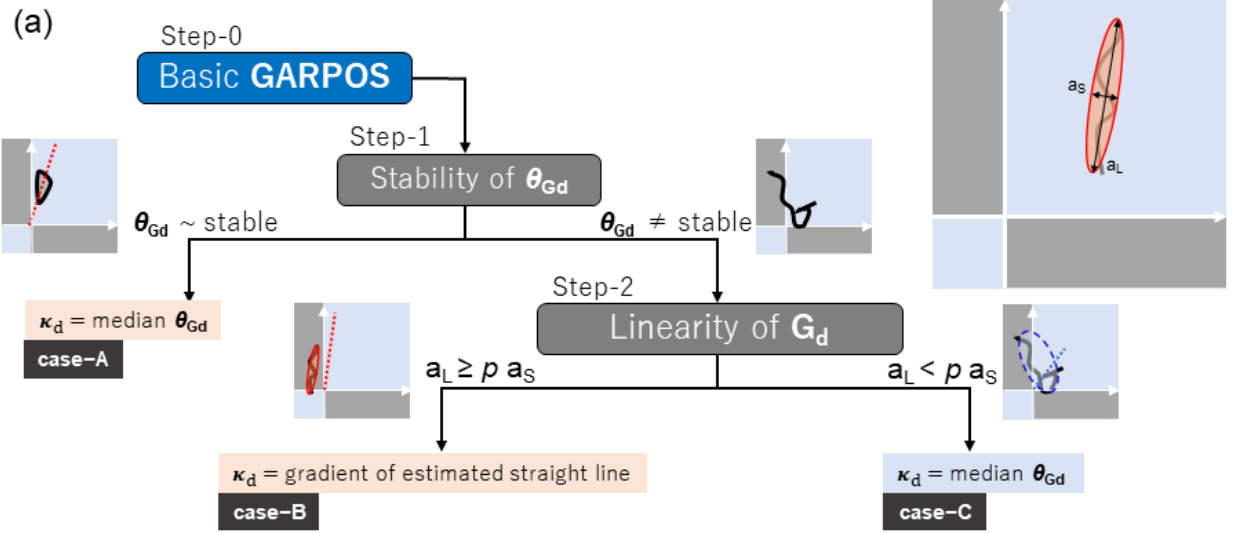
248 The simple constraint assumption proposed in this study improved the accuracy of positioning
 249 solution in many cases, but some outliers still even within the Type-I remain (green-lined circles
 250 in fig. 5b). For example, in 2017-Aug at FUKU, the \mathbf{G}_N trajectory varies with time (fig. 3f). In
 251 this case, our algorithm that fixes one κ_N is considered not reasonable because it failed to
 252 improve the positioning solution. The positioning solution was improved (green circles in fig.
 253 5b) when fixed with multiple κ_N for two divided periods (fig. 3g). The positioning solutions for
 254 some other outlier epochs were similarly improved by assuming two κ_d during observations
 255 (green circles in fig. 5b). In these epochs, the transition of the gradient state might have occurred
 256 in a short time. The large variation in the eastward component of the FUKU time-series suggests
 257 that such temporal change of θ_{GE} might have occurred frequently.

258 For other outlier example, the eastward component of 2017-Dec at FUKU was classified in case-
 259 B, and the estimated positioning solution (purple-lined circle in fig. 5b) was deteriorated. This
 260 cause can be inferred from the actual observation of sound speed profiles (SSPs). Fig. S1
 261 compares SSPs during observations of 2017-Jul at ASZ2 and 2017-Dec at FUKU. The difference
 262 of SSPs at ASZ2 is located at around 100–600 m depth. Although these observations suggest
 263 only 'SSS change over time' and do not explicitly suggest a 'gradient field,' they indicate a
 264 possibility that a gradient change at this depth. This can be regarded as a single layer shallow
 265 gradient at ASZ2 (depth: 2900 m), suggesting that the 2nd-cycle result is more appropriate than
 266 the 1st-cycle result (fig. 3d). On the other hand, the differences of SSPs at FUKU (fig. S1b) are
 267 located at around 100–400 m and 600–1000 m depths. These depths can be regarded as shallow
 268 and deep gradients at FUKU (1250 m). It suggests that validity that \mathbf{G}_N passes the Type-II range
 269 as estimated in the 1st-cycle. In this way, we can narrow down the range of \mathbf{G}_d using the SSP
 270 direct observations and a more reasonable correction of \mathbf{G}_d may be possible.

271 If there is only single gradient source as fig. 4a, $\frac{D_{cE}}{D} = \frac{D_{cN}}{D}$. If there are different gradient sources,
 272 it is possible that the effective gradient layers are different in the eastward and northward
 273 directions. When \mathbf{G}_d is decided in Type-I in the 2nd-cycle, $\frac{D_{cd}}{D}$ is obtained as follow:

$$274 \quad \frac{D_{cd}}{D} = (1 + \kappa_d)^{-1}. \quad (5)$$

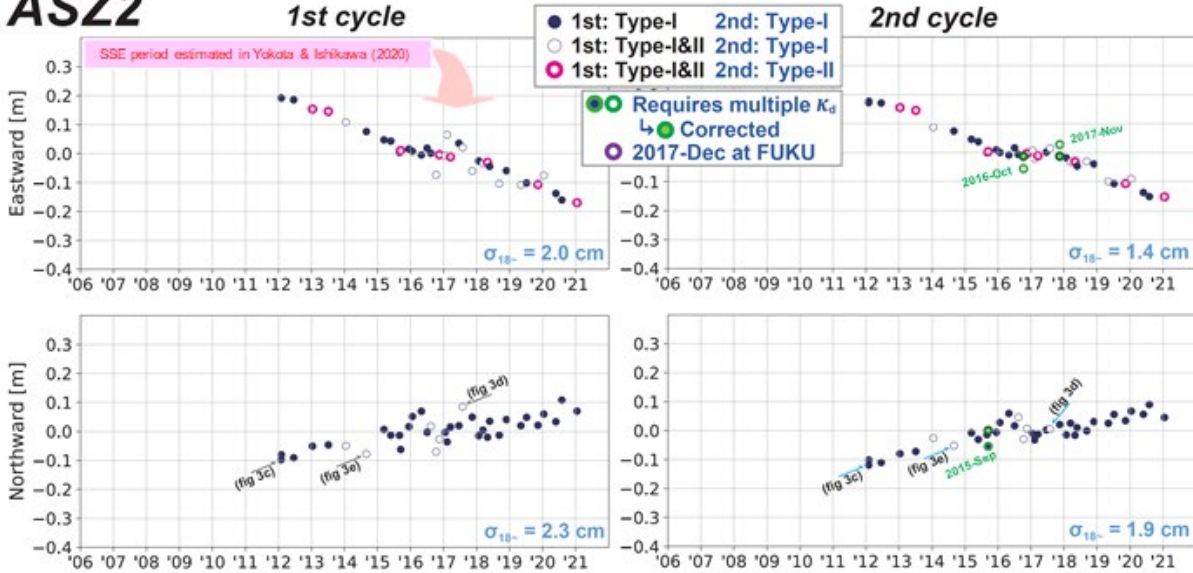
275 Fig. 5d shows plots of $(\frac{D_{cE}}{D}, \frac{D_{cN}}{D})$. Many epochs at ASZ2 were determined in the range of
276 $\frac{D_{cE}}{D} \sim \frac{D_{cN}}{D}$ but about half epochs at FUKU were determined to be outside those ranges. At ASZ2,
277 $\frac{D_{cd}}{D}$ were mostly located at relatively shallower side (0–0.5), suggesting a gradient field due to the
278 Kuroshio. At FUKU, $\frac{D_{cd}}{D}$ were often located at relatively deeper side, suggesting a deep gradient
279 field close to the seafloor and the complexity of the sea condition in the Japan Trench region.
280



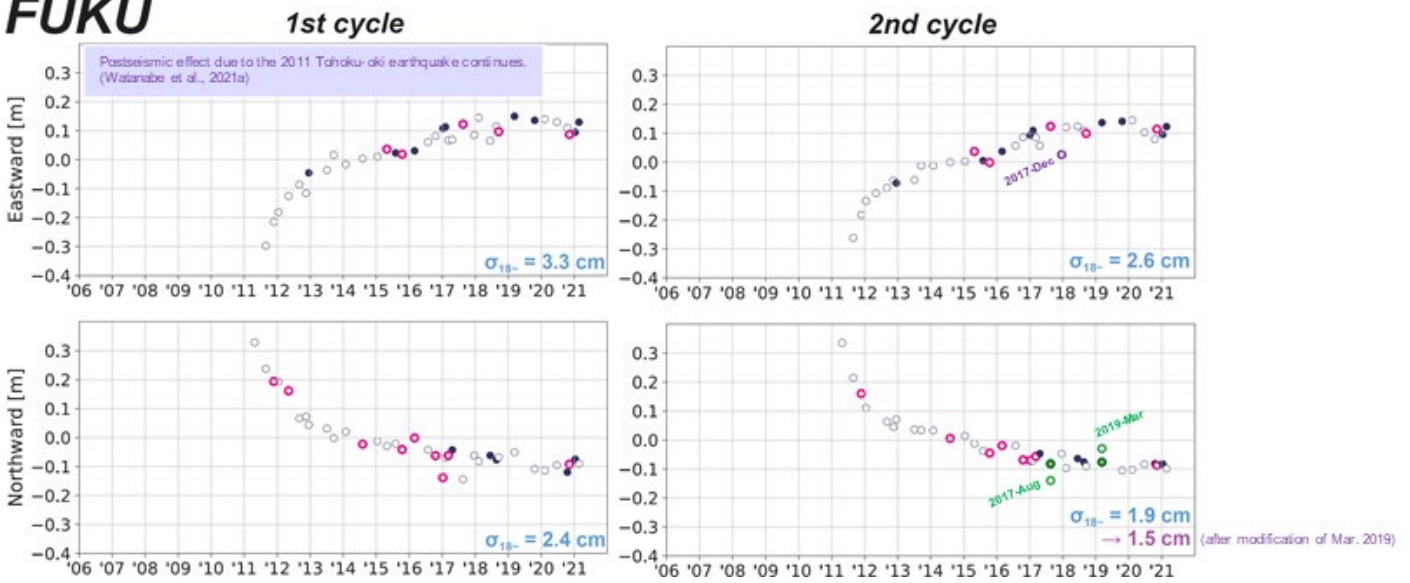
281

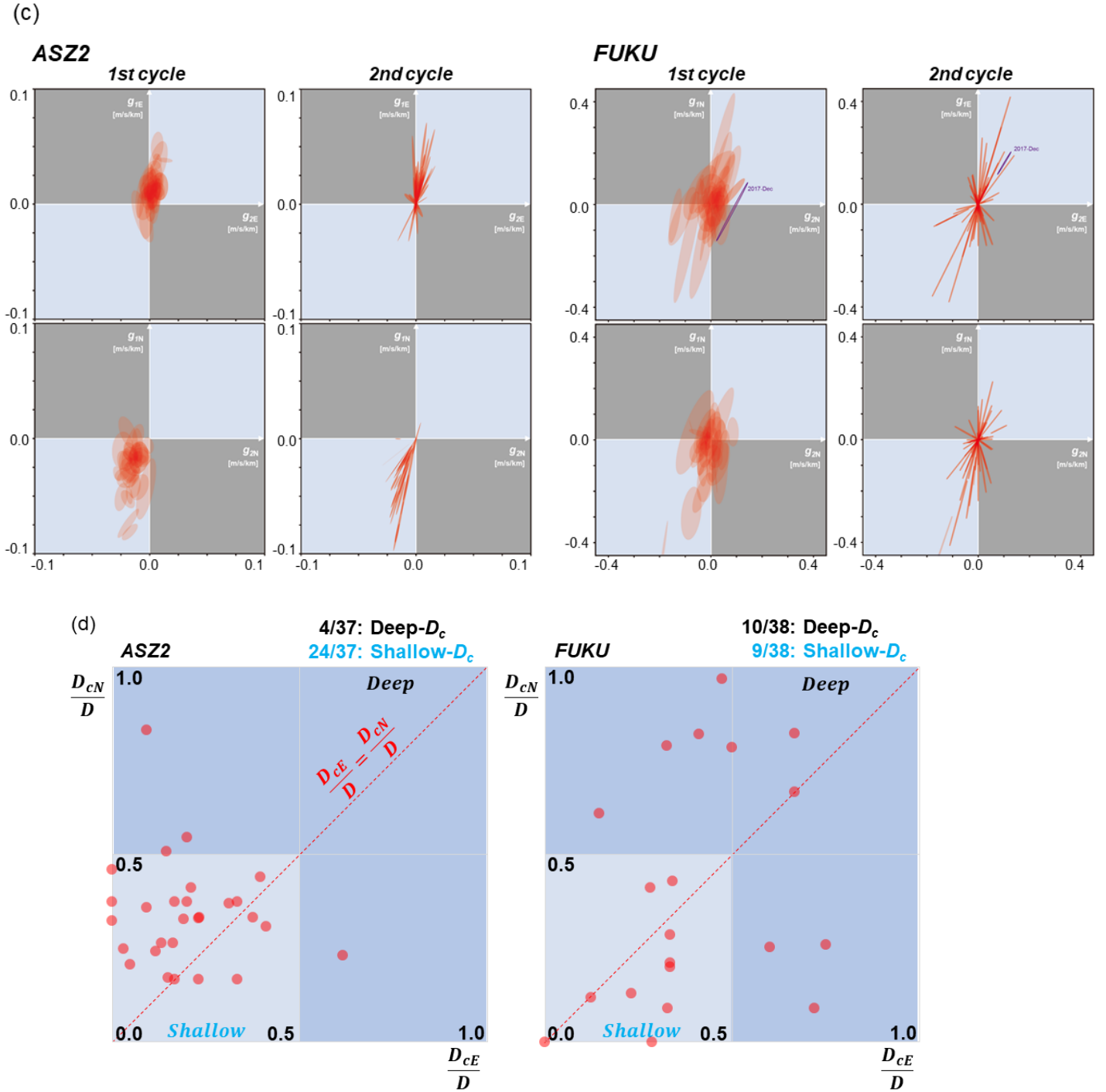
282

(b)
ASZ2



FUKU





284 **Figure 5.** (a) Proposed algorithm flow for determining κ_d considering \mathbf{G}_d changes. (b)
 285 Comparison of the GARPOS ver 1.0.0 solution (1st-cycle) and the 2nd-cycle positioning solution
 286 (ASZ2 and FUKU). The meanings of the circle colors are written in the legend in the graph. The
 287 1σ on the fitted linear trend after 2018 ($\sigma_{18\sim}$) is also written by blue characters. (c) Ranges of \mathbf{G}_d

288 (red ellipses) determined in the 1st- and 2nd-cycles for each epoch. (FUKU) Purple ranges
289 indicate \mathbf{G}_E of 2017-Dec. (d) The plots of $(\frac{D_{cE}}{D}, \frac{D_{cN}}{D})$ estimated in the 2nd-cycle at (a) ASZ2 and
290 (b) FUKU. Red dotted lines indicate $\frac{D_{cE}}{D} = \frac{D_{cN}}{D}$. The numbers at the top are the epoch ratios of
291 $(\frac{D_{cE}}{D} > 0.5) \cup (\frac{D_{cN}}{D} > 0.5)$ (indicating deep- D_c) and $(\frac{D_{cE}}{D} \leq 0.5) \cap (\frac{D_{cN}}{D} \leq 0.5)$ (indicating
292 shallow- D_c). The denominator includes the epochs in Type-II.
293

294 **6 Summary**

295 As a geodetic consequence, we found that the assumption that θ_{Gd} is generally temporal-stable is
296 valid in about 90% epochs excluding some outliers at two sites, and it improves the positioning
297 accuracy. A more appropriate time-series could be obtained by finer determination flow even for
298 the remaining less than 10% epochs. In the future, a more appropriate \mathbf{G}_d correction might be
299 developed using SSP direct observations and frequency of complex SSS generation as the
300 preliminary information. Instead of a secondary solution as in this paper, a method for finding a
301 unique solution e.g., by a modification of GARPOS, which explicitly considers the temporal-
302 stability of \mathbf{G}_d , might be also developed. The time-stability of \mathbf{G}_d is also one of the keys for
303 understanding the tendency of narrow km-scale ocean fields in the open ocean. In particular, it is
304 valuable in marine acoustic engineering and may contribute to its future development.

305

306 **Acknowledgments**

307 This study was supported by ERI JURP 2021-Y-KOBO25 in Earthquake Research Institute, the
308 University of Tokyo. Figure 1c was prepared using Generic Mapping Tools (Wessel et al., 2019).

309

310 **Data Availability Statement**

311 The GNSS-A data and analysis software “GARPOS v1.0.0” are available at Zenodo (Japan
312 Coast Guard, 2021; Watanabe et al., 2021b); (<https://doi.org/10.5281/zenodo.5802560> and
313 <https://doi.org/10.5281/zenodo.4522027>).

314 **References**

- 315 Asada, A., and Yabuki T. (2001). Centimeter-level positioning on the seafloor. *Proc. Jpn. Acad.*
316 *Ser B* 77, 7–12, <https://doi.org/10.2183/pjab.77.7>
- 317 Fujita, M., Ishikawa, T., Mochizuki, M., Sato, M., Toyama, S., Katayama, M., Kawai, K.,
318 Matsumoto, Y., Yabuki, T., Asada, A., and Colombo, O. L. (2006). GPS/Acoustic seafloor
319 geodetic observation: method of data analysis and its application. *Earth Planet. Space* 58, 265–
320 275, <https://doi.org/10.1186/BF03351923>
- 321 Geng, J., Jiang, P., and Liu, J. (2017). Integrating GPS with GLONASS for high-rate
322 seismogeodesy. *Geophys. Res. Lett.*, 44, 3139–3146. <https://doi.org/10.1002/2017GL072808>
- 323 Japan Coast Guard (2021). GNSS-A data obtained at the sites along the Japan Trench from March
324 2011 to January 2021. *Zenodo*, <https://doi.org/10.5281/zenodo.5802560>
- 325 Kinugasa, N., Tadokoro, K., Kato, T., and Terada, Y. (2020). Estimation of temporal and spatial
326 variation of sound speed in ocean from GNSS-A measurements for observation using moored buoy.
327 *Prog. Earth Planet. Sci.* 7, 21. <https://doi.org/10.1186/s40645-020-00331-5>
- 328 Sato, M., Ishikawa, T., Ujihara, N., Yoshida, S., Fujita, M., Mochizuki, M., and Asada, A. (2011).
329 Displacement above the hypocenter of the 2011 Tohoku-oki earthquake. *Science* 332, 1395.
330 <https://doi.org/10.1126/science.1207401>
- 331 Spiess, F. (1985). Suboceanic geodetic measurements. *Geosci. Remote Sensing*, GE-23(4),
332 502–510, <https://doi.org/10.1109/TGRS.1985.289441>
- 333 Watanabe, S., Bock, Y., Chadwell, C. D., Fang, P., and Geng, J. (2017). Long-term stability of the
334 kinematic Precise Point Positioning for the sea surface observation unit compared with the baseline
335 analysis. *Rep. Hydro. Ocean. Res.* 54, 38–73

- 336 Watanabe, S., Ishikawa, T., Yokota, Y., and Nakamura, Y. (2020). GARPOS: Analysis software
337 for the GNSS-A seafloor positioning with simultaneous estimation of sound speed structure. *Front.*
338 *Earth Sci.* 8, 597532, <https://doi.org/10.3389/feart.2020.597532>
- 339 Watanabe, S., Ishikawa, T., Nakamura, Y., and Yokota, Y. (2021a). Co- and postseismic slip
340 behaviors extracted from decadal seafloor geodesy after the 2011 Tohoku-oki earthquake. *Earth*
341 *Planets Space* 73, 162. <https://doi.org/10.1186/s40623-021-01487-0>
- 342 Watanabe, S., Ishikawa, T., Yokota, Y., and Nakamura, Y. (2021b). GARPOS: Analysis tool for
343 GNSS-Acoustic seafloor positioning (Version 1.0.0). *Zenodo*,
344 <https://doi.org/10.5281/zenodo.4522027>
- 345 Wessel, P.L., Luis, J.F., Uieda, L., Scharroo, R., Wobbe, F., Smith, W. H. F., and Tian, D. (2019).
346 The Generic Mapping Tools version 6. *Geochem. Geophys. Geosyst.* 20, 5556–5564.
347 <https://doi.org/10.1029/2019GC008515>
- 348 Yasuda, I., Okuda, K., Shimizu, Y. (1996). Distribution and modification of north Pacific
349 intermediate water in the Kuroshio–Oyashio interfrontal zone. *J. Phys. Oceanogr.*, 26, 448–465.
350 [https://doi.org/10.1175/1520-0485\(1996\)026<0448:DAMONP>2.0.CO;28](https://doi.org/10.1175/1520-0485(1996)026<0448:DAMONP>2.0.CO;28)
- 351 Yokota, Y., Ishikawa, T., Watanabe, S., Tashiro, T., and Asada A. (2016). Seafloor geodetic
352 constraints on interplate coupling of the Nankai Trough megathrust zone. *Nature* 534, 374–377.
353 <https://doi.org/10.1038/nature17632>
- 354 Yokota, Y., Ishikawa, T., and Watanabe, S. (2018). Seafloor crustal deformation data along the
355 subduction zones around Japan obtained by GNSS-A observations. *Sci. Data* 5, 180182.
356 <https://doi.org/10.1038/sdata.2018.182>
- 357 Yokota, Y. (2019). Quantitative interpretation of the ability of the GNSS-A to monitor underwater
358 structure. *J. Marine Acoust. Soc. Jpn.* 46, 3, 116–129. <https://doi.org/10.3135/jmasj.46.116>

359 Yokota, Y., and Ishikawa, T. (2019). Gradient field of undersea sound speed structure extracted
360 from the GNSS-A oceanography: GNSS-A as a sensor for detecting sound speed gradient. *SN*
361 *Applied Sciences* 1, 693. <https://doi.org/10.1007/s42452-019-0699-6>

362 Yokota, Y., Ishikawa, T., and Watanabe, S. (2019). Gradient field of undersea sound speed
363 structure extracted from the GNSS-A oceanography. *Mar. Geophys. Res.* 40, 493–504.
364 <https://doi.org/10.1007/s11001-018-9362-7>

365 Yokota, Y., and Ishikawa, T. (2020). Shallow slow slip events along the Nankai Trough detected
366 by GNSS-A. *Sci. Adv.* 6, eaay5786. <https://doi.org/10.1126/sciadv.aay5786>

367 Yokota, Y., Ishikawa, T., Watanabe, S., and Nakamura, Y. (2020). Kilometer-scale sound speed
368 structure that affects GNSS-A observation: case study off the Kii channel. *Front. Earth Sci.* 8, 331.
369 <https://doi.org/10.3389/feart.2020.00331>

370 Yokota, Y., Ishikawa, T., Watanabe, S., and Nakamura, Y. (2021). Crustal deformation detection
371 capability of the GNSS-A seafloor geodetic observation array (SGO-A), provided by Japan Coast
372 Guard. *Prog. Earth Planets Sci.* 8:63. <https://doi.org/10.1186/s40645-021-00453-4>

373